Crystallographic Texture Evolution of a Zinc Sheet Subjected to Different Strain Paths

FERNANDO SCHLOSSER, CLAUDIO SCHWINDT, VALERIA FUSTER, ANDREA TOMMASI, and JAVIER WALTER SIGNORELLI

The use of zinc sheets has largely increased in the last years, fundamentally because of new tendencies in architecture and, at the same time, due to its excellent properties, as corrosion resistance under aggressive climatic conditions, malleability, recyclability, and surface finishing aspect. In the present work, the X-ray diffraction technique is used to characterize the crystallographic texture evolution of a strongly anisotropic Zn20 zinc sheet (Zn-Cu-Ti) subjected to uniaxial tension, plane strain, and equibiaxial tension, for specimens cut at 0, 45, and 90 deg with respect to the rolling direction. The crystallographic texture evolution is evaluated by means of pole figures, orientation distribution function, and Kearns factors. For all tested strain paths, deformation produces a decrease in the intensity of the crystallographic textures, due to a dispersion of the orientations of the different axes around the initial maxima.

I. INTRODUCTION

ZINC sheets are characterized for having great surface aspect and for being malleable and recyclable. Zinc is also naturally resistant to corrosion, durable, and does not require costly maintenance. These qualities make zinc sheets suitable for a large variety of uses in the architectural industry. It can be seen in roofs, facades, rainwater systems, and multiple other uses, in particular where climatic conditions are severe. Zinc sheets are produced by continuous casting followed by rolling until the final thickness.

A distinctive characteristic of rolled HCP materials is the development of typical crystallographic textures. The various possible typical textures are determined by the c/a lattice relation of the material, compared to the ideal value of 1.633.[1] In the case of zinc, its c/a relation is 1.856, which results in a rolling texture characterized by concentration of the basal poles in the plane normal to the transverse direction. The most densely packed directions in zinc crystals are the $\langle 11\bar{2}0 \rangle$ directions, which are contained in the basal $\{0002\}$, prismatic $\{10\bar{1}0\}$, and pyramidal $\{10\bar{1}1\}$ planes. The most active slip system at room temperature is the basal system, formed by dislocations gliding in the $\langle 11\bar{2}0 \rangle$ directions on the $\{0002\}$ planes. The second most active slip system is the pyramidal π_2, formed by glide in the $\langle 11\bar{2}3 \rangle$ directions on the $\{11\bar{2}2\}$ planes.[2,3]

The combined effect of crystallographic texture, crystalline structure, and microstructure results in a very strong mechanical anisotropy.[4] Recently, Schwindt et al.[5] used a viscoplastic self-consistent scheme to reproduce the anisotropy on the stress–strain curves of a Zn20 sheet, showing that texture evolution plays an important role on both mechanical anisotropy and formability.

Previous studies focused on the analysis of crystallographic texture evolution of zinc sheets during rolling. Philippe et al.[6] studied the texture evolution of a zinc-copper-titanium sheet after cold rolling, and found the presence of two components usually reported in the literature,[7,8] and two other components not mentioned before. Diot et al.[9] observed a through-thickness texture gradient after cold rolling of a zinc-copper-titanium sheet as a consequence of shear stress and friction on the surface. Later, Diot et al.[10] observed that the heterogeneity in distribution of aluminum in zinc-copper-titanium sheets strengthens the through-thickness texture gradient produced by rolling. Zhang et al.[11] found that sharper textures are developed on the fast side of asymmetric with respect to symmetric rolling of a Zn-Cu-Ti sheet. Solas et al.[12] used an N-site viscoplastic model with recrystallization to simulate the deformation and to predict the texture evolution of high-purity zinc polycrystals. Faur and Cosmeleață[13] found that alloying Zn with Cu and Ti decreases the amount of twinning, while increasing the amount of both Cu and Ti suppresses twinning and enhances a grain refinement process by the presence of the secondary phase TiZn15. These works have focused on the texture evolution produced by rolling, leaving aside the analysis of texture evolution in typical sheet forming

FERNANDO SCHLOSSER and CLAUDIO SCHWINDT are with the Department of Engineering, UNS-CONICET, Av. Alem 1253, Bahía Blanca (B8000CPB), Buenos Aires, Argentina. VALERIA FUSTER and JAVIER WALTER SIGNORELLI are with the IFIR-UNR-CONICET, Bv. 27 de Febrero 210b, Rosario (S2000BTP), Santa Fe, Argentina. Contact e-mail: signorelli@ifir-conicet.gov.ar ANDREA TOMMASI is with the Géosciences Montpellier - CNRS and Université de Montpellier, Place Eugene Bataillon, Montpellier, France.

deformation conditions. The present study focuses on this aspect.

The aim of the present work is to evaluate the evolution of the crystallographic texture of a 0.65-mm-thick Zn20 zinc sheet as a result of uniaxial tension (UAT), plane strain (PS), and equibiaxial tension (EBA) tests for specimens cut at 0 deg (rolling direction, RD), 45 deg (diagonal direction, DD), and 90 deg (transverse direction, TD) to the rolling direction. These conditions represent some of the different forming processes used in industry. Pole figures are analyzed and quantitatively compared by means of the Kearns factors. Orientation distribution function (ODF) sections for $\varphi_2 = 0$ and 30 deg are also discussed. In addition, Rietveld refinement was conducted in order to determine the amount of $TiZn_{16}$ precipitates, as well as to ascertain crystallographic and microstructural properties of the alloy, such as the accumulated microstrain and crystallite size.

II. MATERIAL AND METHODS

The chemical composition of the alloy is Zn-0.094Cu-0.047Ti wt pct. Due to the high solubility of Cu in Zn at ambient temperature (0.3 wt pct), Cu is found in substitutional solid solution.[14] On the other hand, Ti has low solubility in Zn. It forms a Zn-rich intermetallic hard phase $TiZn_{16}$, which precipitates in the shape of thin bands.[15]

The microstructure of the initial material, characterized by optical microscopy, is highly heterogeneous, as illustrated in Figure 1, which shows micrographs of two neighboring zones of the same initial sheet as indicated in the figure insets. The intermetallic compound $TiZn_{16}$ has a dark contrast and an elongated shape in the rolling direction. Its volume fraction was determined by Rietveld refinement of the diffraction patterns, discussed in Section III–A; it is ≤3 vol pct. The presence of an oriented elongated intermetallic phase induces another mechanical anisotropy component (in addition to the

texture-induced one), modifying the Zn20 sheets' mechanical resistance and formability.

To quantify the mechanical anisotropy of the material, uniaxial tension tests were performed at room temperature on samples cut in three orientations with respect to RD: 0, 45, and 90 deg. The strain rate was set to $5 \times 10^{-4} s^{-1}$. True stress–true strain curves are shown in Figure 2. Maximum true stresses are 184 MPa in RD, 209 MPa in DD (13.6 pct higher than in RD), and 246 MPa in TD (33.7 pct higher than in RD), clearly showing a dependence on the orientation of the
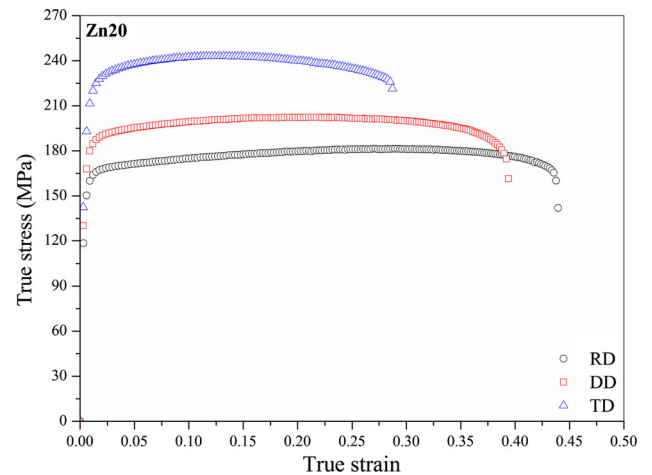

Fig. 2—True stress–true strain curves for the three sheet orientations.

Table I. Lankford Coefficients for the Three Sheet Orientations

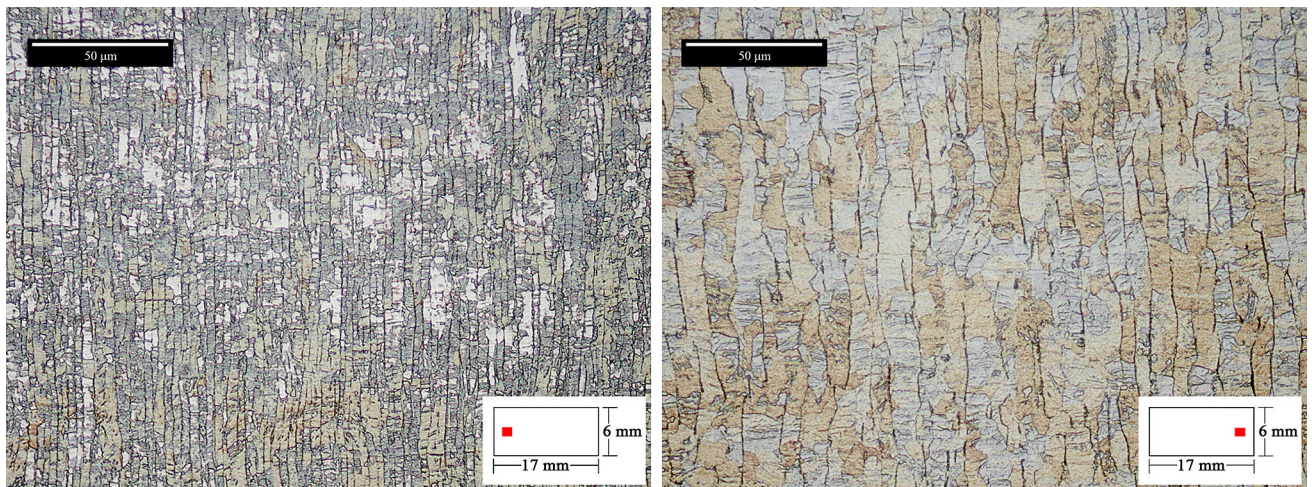| Angle to RD (deg)	Lankford Coefficient
0	0.258
45	0.419
90	0.544

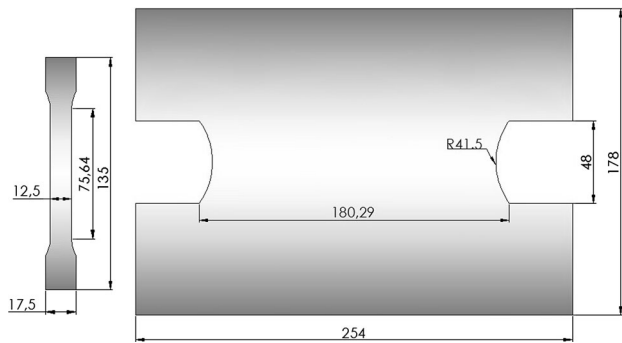Fig. 1—Optical micrographs of the RD–TD plane with the RD aligned vertically (500 times).

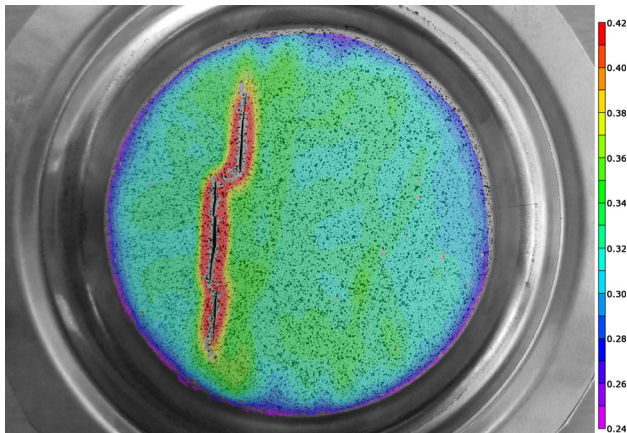Fig. 3—Sample geometries employed: UAT (left); PS (right).

Fig. 4—Distribution of the major strain in a Marciniak specimen, measured by the DIC technique.
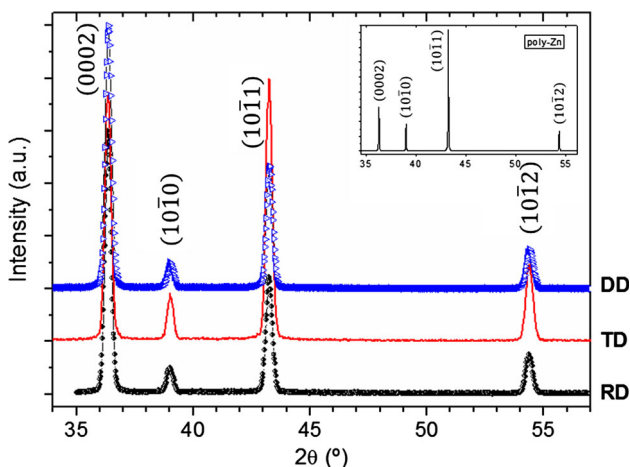

Fig. 5—X-ray patterns of the UAT RD, TD, and DD specimens. Only Zn reflections are indicated by the Miller indexes. Inset: polycrystalline pure Zn X-ray pattern, *i.e.*, with random texture.

sheet. The maximum longitudinal strain also depends on the orientation, being 50 and 33 pct higher in RD and DD, respectively, with respect to TD.

Additional tensile tests were performed to determine the Lankford coefficients at 20 pct of engineering strain. Results are shown in Table I. As expected, the values are below unity, which implies that the sheet is not suitable for deep drawing.[16]

It is known that mechanical properties are strongly related to the crystallographic texture of materials. This correlation is particularly important in alloys with hexagonal crystal structures. This is due to the reduced number of available slip systems, in comparison with FCC and BCC cubic structures. The tension tests described above confirm these predictions. However, since the texture evolves during deformation, this effect will also depend on the strain path and, more specifically, on the rate of texture evolution in each path.

We analyze therefore the texture evolution on three strain paths, UAT, PS, and EBA, which correspond to strain paths observed in standard sheet forming processes. UAT and PS tests were performed with tensile tests, the first ones with regular ISO50 samples (Figure 3, left) and the latter ones with samples of a specific geometry (Figure 3, right). EBA tests were conducted with Marciniak tests on 200-mm-diameter circular samples. For UAT and PS tests, samples were cut in RD, DD, and TD. This is not necessary in the case of EBA, where all directions are solicited simultaneously. The end of the tests was defined by the onset of localized necking.

The strain in each sample was determined by the digital image correlation (DIC) technique.[17] This technique measures deformation in a non-invasive way using images of the sample acquired before and after deformation. It works by dividing the reference image into small subsets, which are correlated on the deformed image. To uniquely identify each subset, the sample requires a random pattern, which is artificially generated by painting black spots on a white-painted background. The technique allows calculating the strain field in the sample (Figure 4).

Crystallographic textures were measured in samples extracted from a homogeneous strain zone as close as possible to the necking domain. The diffraction patterns and pole figures were measured with a Phillips X'Pert Pro-MPD system, using CuKα radiation. The diffractometer was equipped with a X-ray lens optics, parallel plaques, and an Eulerean Cradle for texture measurements. The diffractograms were collected from 30 to 60 deg, in 0.02 deg angular 2θ steps, with 1 second collecting time. Sufficient statistics was acquired for refinement purposes. Rietveld refinement of X-ray diffraction patterns was done using the Maud software, including microstructural and texture analysis into the traditional refinement.[18] The standard chosen to account for instrument artifacts was LaB_6.[19] To account for texture, the intensity correction of the X-ray spectra was performed using the harmonic model implemented in Maud. The crystallite size D_{hkl} and accumulated microstrain ($\langle\varepsilon\rangle^{1/2}$) due to perfect dislocations were obtained using the Popa model,[20] which is suitable for anisotropic properties.

Pole figures (PFs) were obtained at 2θ angles of 36.5, 39.1, 43.4, and 54.5 deg, corresponding to Zn {0002}, {10$\bar{1}$0}, {10$\bar{1}$1}, and {10$\bar{1}$2} diffraction reflections, using a 5 mm × 5 mm grid. Each measurement was
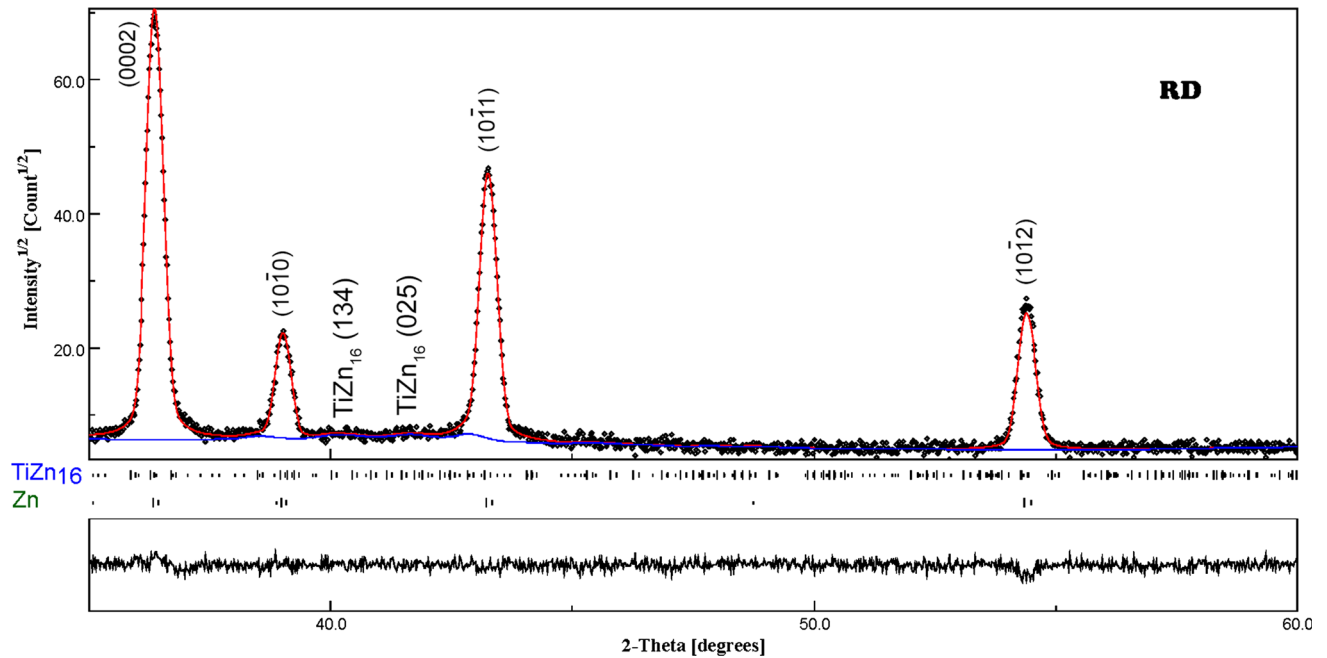
Fig. 6—Rietveld refinement output graphic from the UAT RD specimen. Reflections from each phase are represented in different colors: Zn (green) and TiZn$_{16}$ (blue). Upper part: X-ray measurement superimposed over the refined curve; middle part: vertical bars representing the 2θ reflections of each phase; lower part: differences between the experimental pattern and the calculated profile (residual curve) using Maud (Color figure online).

Table II. Phase Quantification and Lattice Parameters of UAT RD, TD, and DD Samples Determined by Rietveld Refinement

Sample	Phases	Weight Percent	Lattice Parameters (nm)			
			a	b	c	c/a
UAT RD	Zn	97	0.2681	0.2681	0.4970	1.85
	TiZn$_{16}$	3	0.7735	1.1494	1.1834	
UAT TD	Zn	99	0.2681	0.2681	0.4970	1.85
	TiZn$_{16}$	1	0.7735	1.1496	1.1834	
UAT DD	Zn	98	0.2681	0.2681	0.4969	1.85
	TiZn$_{16}$	2	0.7810	1.1431	1.1849	

Table III. Zn Microstructural Parameters in UAT RD, TD, and DD Samples Determined by Rietveld Analysis

Sample	Crystallographic Planes ($hkil$)		Crystallite Size, D_{hkl} (nm)	Microstrain ($\langle \varepsilon \rangle^{1/2}$)	GOF
UAT RD	(0002)	basal	390	1.3×10^{-3}	
	(10$\bar{1}$0)	prismatic	240	—*	1.18
	(10$\bar{1}$1)	pyramidal I	270	2×10^{-4}	
UAT TD	(0002)	basal	290	1.4×10^{-3}	
	(10$\bar{1}$0)	prismatic	190	4×10^{-5}	1.17
	(10$\bar{1}$1)	pyramidal I	210	4×10^{-4}	
UAT DD	(0002)	basal	330	1.2×10^{-3}	
	(10$\bar{1}$0)	prismatic	290	3×10^{-4}	1.22
	(10$\bar{1}$1)	pyramidal I	290	2×10^{-4}	

* Means negligible.

done from $\varphi = 0$ to 85 deg in 5 deg steps, while rotating the sample 360 deg around ND in 5 deg steps, with an exposure time of 1 second per step. During the exposure, the sample was translated along the horizontal axis from −5 to + 5 mm, to increase the volume average and grain statistics. Experimental PFs were corrected for background and defocussing. Subsequently, the ODF was calculated and the PFs were recalculated using the Matlab® open-source toolbox MTEX.[21] Hexagonal crystal structure was assumed (6/mmm) and an
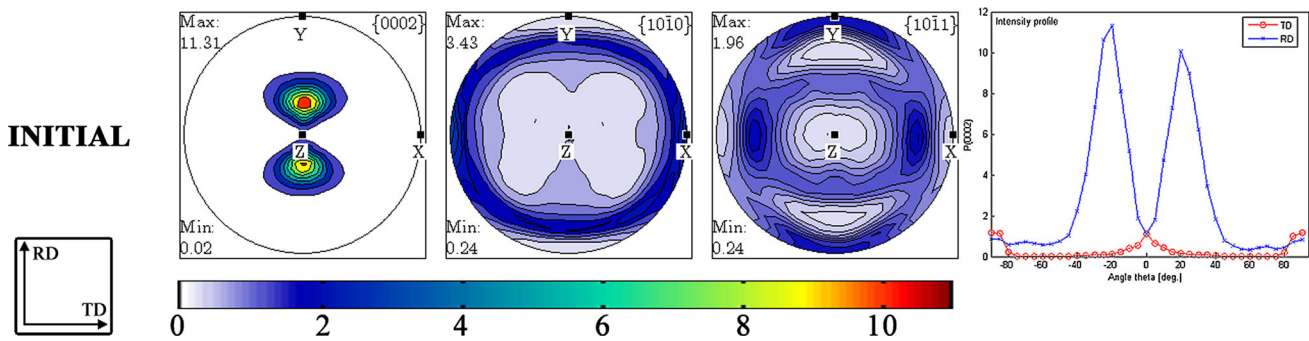
Fig. 7—Pole figures of the as-received sheet and intensity profiles of the basal poles with respect to RD and TD.

Table IV. Kearns Factors for All the Samples

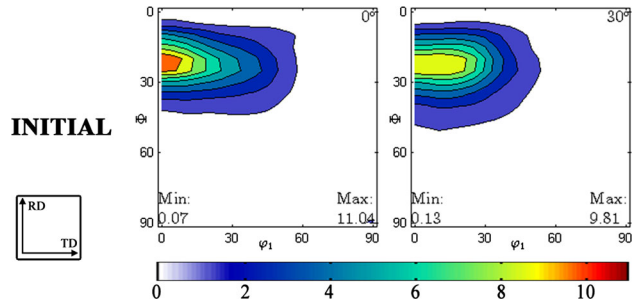| Texture	f_{RD}	f_{TD}	f_{ND}
Initial	0.264	0.156	0.580
UAT RD	0.197	0.209	0.594
UAT DD	0.223	0.199	0.578
UAT TD	0.152	0.266	0.582
PS RD	0.274	0.195	0.531
PS DD	0.287	0.200	0.513
PS TD	0.294	0.222	0.484
EBA	0.265	0.197	0.538

Fig. 8—Sections of the ODF for $\varphi_2 = 0$ deg (left) and $\varphi_2 = 30$ deg (right) for the as-received sheet.

orthorhombic symmetry was considered for the sample. In contrast to cubic structure materials, the texture of low crystal symmetry materials can be characterized by the use of different indexes and/or coefficients. To measure the severity of texture, one option is the J-index, which is mathematically defined as the second moment of an ODF. This index is calculated as the normalized sum of the squared values of the C-coefficients of the harmonic expansion of the ODF.[22] It ranges between 1 for a randomly textured material and ∞ for a single crystal. However, it is more usual to characterize the textures of hexagonal materials by three values known as Kearns factors.[23] They are a weighted average of the intensity of the basal poles figure with respect to the sample directions and are defined as

$$f = \frac{\int_0^\pi I(\theta)\cos^2(\theta)\sin(\theta)d\theta}{\int_0^\pi I(\theta)\sin(\theta)d\theta},$$

where $I(\theta)$ is the average basal pole figure intensity at an angle θ from a given sample direction, *i.e.*, RD, TD, and ND.

III. RESULTS AND DISCUSSION

A. *X-ray Diffraction Analysis*

The diffractograms of samples deformed in UAT in RD, TD, and DD orientations are shown in Figure 5. HCP Zn is the major component of the matrix. The main crystallographic reflections of Zn phase are labeled by their Miller indexes. The space group is *P63/mmc* (# 198), hP2 Pearson symbol (JCPDS card No. 04-831, ICSD No. 64990). The differences in relative intensities are attributed to the texture developed in each sample.

The diffractograms of all the samples show that the major component of the alloy is Zn, but broad and low-intensity reflections of $TiZn_{16}$ are also observed. This is in accordance with the quantification analysis. By comparison with the X-ray pattern of non-textured polycrystalline Zn, shown in the inset of Figure 5, we see that the relative intensity of the Zn reflections changes due to texture development during rolling followed by UAT. The intensity of the {0002} basal planes peak increases and there is a marked reduction of intensity of
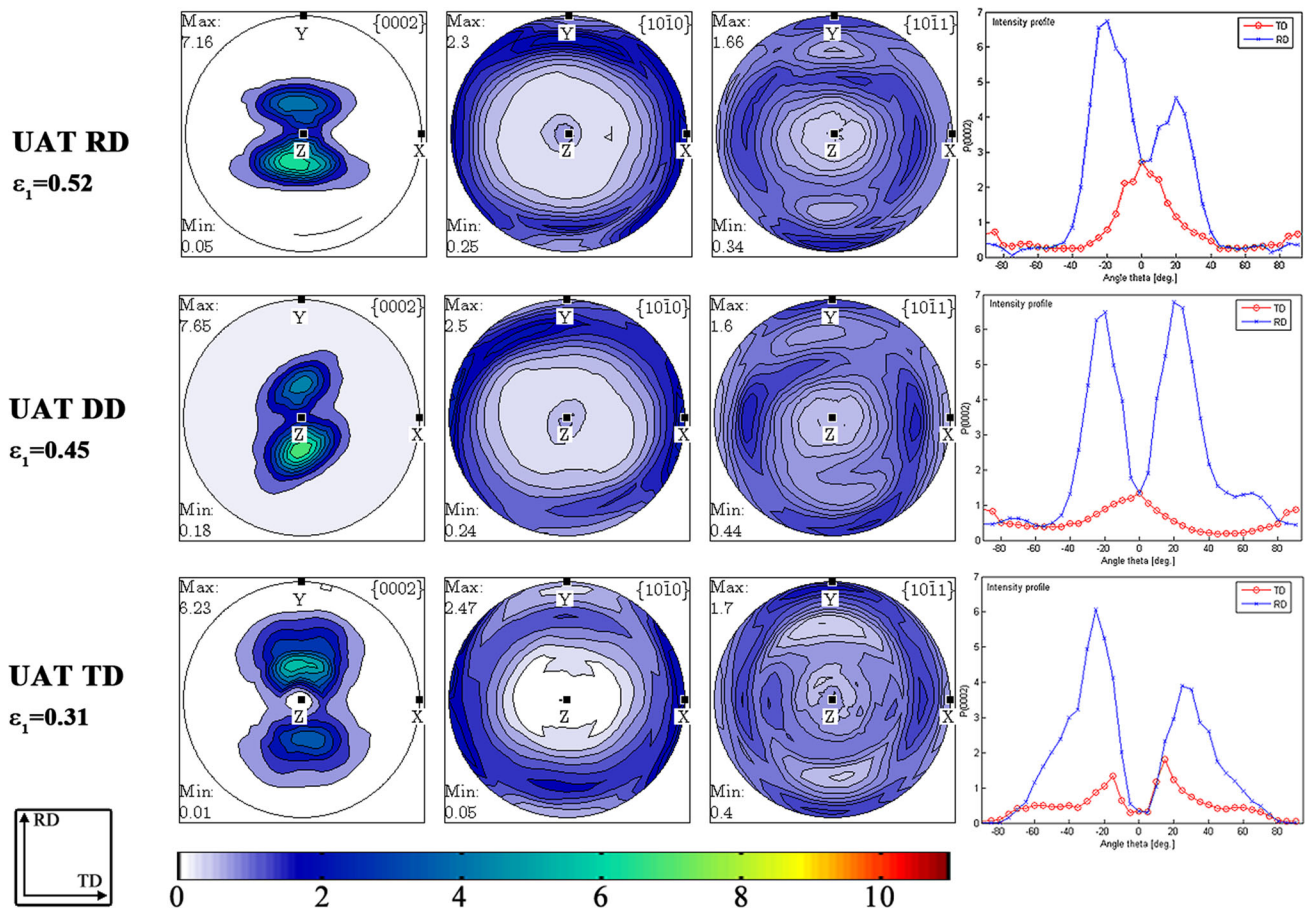
Fig. 9—Pole figures of the UAT samples and intensity profiles of the basal poles with respect to RD and TD.

the $\{10\bar{1}1\}$ reflection. Interestingly, these changes are less marked for the TD specimen.

A minor amount of precipitates have been identified as $TiZn_{16}$. The high-intensity reflections of this intermetallic can be better appreciated in Figure 6, where the y-axis scale represents the square root of intensity in order to enhance smaller features of X-ray patterns. The corresponding Miller indexes are indicated for the most intense observed peaks. This intermetallic has an orthorhombic structure, with the Pearson symbol oC68, and a space group $Cmcm$ (# 63) (ICSD #106186).[24]

Rietveld refinement was conducted in order to determine the amount of $TiZn_{16}$ precipitates, as well as to ascertain crystallographic and microstructural properties of the alloy. The refinement results indicate that the sheets are at least 97 wt pct pure in Zn. Phase quantification and refined lattice parameters are presented in Table II. The refined values of crystallite size and accumulated microstrain are summarized in Table III. The quality of the refinements is similar, according to the Goodness of Fit (GoF). Figure 6 shows the graphical results of the Rietveld refinement for the RD specimen.

The evaluated c/a relation confirms the value of 1.856, resulting in an elongated hexagonal unit cell along the c-axis. Similar values of crystalline domain size (D_{hkl}) and accumulated microstrain ($\langle \varepsilon \rangle^{1/2}$) of Zn phase are found in UAT RD, TD, and DD samples. In general, crystallites are slightly larger in the basal plane. Substantial microstrain is developed in response to the mechanical tests, i.e., a raise of the density of perfect dislocations is observed due to the high stresses applied to the material.

For the $TiZn_{16}$ minor phase, the microstructure was assumed to be isotropic. Considering the scarce amount of this intermetallic, refinement deviations must be taken into account. Hence, refined average crystallite
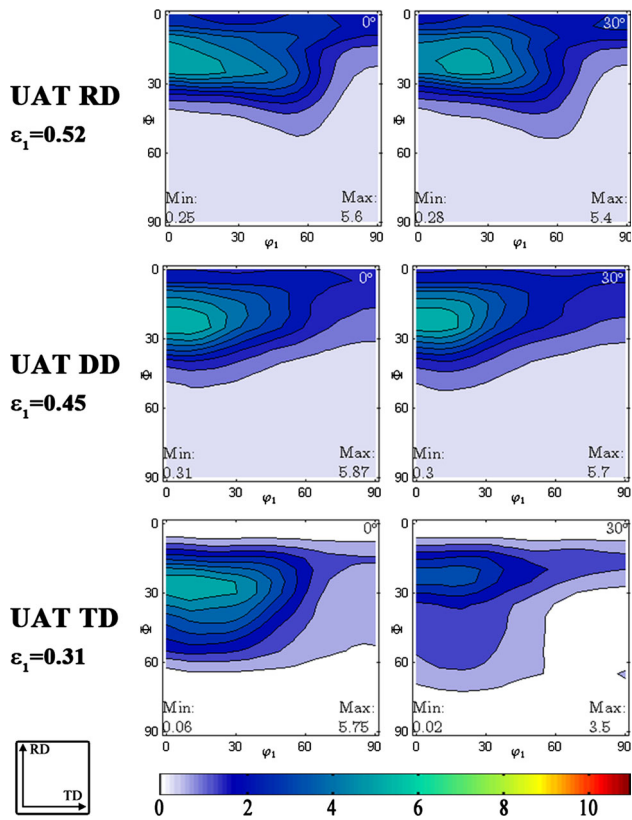
Fig. 10—Sections of the ODF for $\varphi_2 = 0$ deg (left) and $\varphi_2 = 30$ deg (right) for the UAT samples.

size is reported to be in the order of 10 to 20 nm, whereas microstrain ranges from 2×10^{-4} to 1×10^{-3}.

B. Crystallographic Texture Analysis

Crystallographic textures are described and analyzed in terms of the $\{0002\}$, $\{10\bar{1}0\}$, and $\{10\bar{1}1\}$ poles figures, Kearns factors, and ODF sections at $\varphi_2 = 0$ deg and $\varphi_2 = 30$ deg in the Euler space, following Bunge's notation. For HCP materials, the texture is well described by these φ_2 sections.[25] The initial texture of the sheet has the typical characteristics of a rolled HCP material with a c/a value higher than the ideal one. The basal pole figure (Figure 7) shows the basal directions $\langle 0002 \rangle$ concentrated in the ND–RD plane, with an approximate tilting of 20 deg with respect to ND and a maximum intensity of 11.3. The prismatic directions $\langle 10\bar{1}0 \rangle$ are more axisymmetrically distributed

with respect to ND, with a slight tendency to concentrate around TD. The calculated Kearns factors are $f_{RD} = 0.264$, $f_{TD} = 0.156$, and $f_{ND} = 0.580$. For a randomly textured material, Kearns factors are $f_{RD} = f_{TD} = f_{ND} = 1/3$. Table IV resumes their values for all the cases analyzed.

Analyzing the φ_2 ODF sections of the as-received sheet in Figure 8, it is observed that the initial texture is sharp, mainly concentrated at $\varphi_1 = 0$ deg, $\phi = 20$ deg for both $\varphi_2 = 0$ deg and $\varphi_2 = 30$ deg. High intensities were determined for both sections: 11.04 and 9.81, respectively. Thus, the ODF is composed of a basal $\{hkil\}$ fiber along φ_2, where the basal planes are tilted symmetrically $\sim\pm20$ deg with respect to the ND, in the RD–ND plane.

The pole figures corresponding to the UAT RD sample (Figure 9) show that the maximum intensities of basal poles keep their orientation with respect to ND (~20 deg), but the intensities decrease. This decrease results from a dispersion of the basal poles by rotations around both the TD and the ND directions, leading to higher concentrations near ND. This is evidenced by the value in the center shown in the intensity profiles in Figure 9 (upper right), and is also reflected by an increase of f_{ND}. Due to the dispersion of the poles in TD, it can also be observed that f_{TD} grows at the expense of f_{RD}. Similar trends are found for the UAT sample along DD. The TD sample is slightly different, with the peaks of the basal poles at ~25 deg from ND in RD–ND. This results in two peaks in the f_{TD} intensity profile in Figure 9 (lower right), which contrasts with the single peak for the two other orientations.

The ODF sections of the UAT samples are illustrated in Figure 10. They show, in concordance with the PFs, that crystallographic textures are less intense with respect to the as-received sheet. Although texture clearly evolves during the deformation, the changes are mainly in terms of redistribution and dispersion around the main basal texture component, $i.e.$, ~20 to 25 deg rotation around ND. Additionally, while UAT RD and DD samples clearly have the presence of the $\{0001\}$ basal fiber, these orientations are no longer stable in TD and displace to higher values of ϕ, $i.e.$, $\{hkil\}$ fiber. Furthermore, as opposed to UAT RD, the orientations distribution around the maximum exhibits a higher spread in RD, with the fiber extending to $\phi = 60$ deg.

Figure 11 shows the pole figures and the intensities profiles of the basal poles for the PS samples. The intensity of the basal poles in the RD sample slightly diminishes, but maintains the angle to ND, which produces lower f_{ND} values. f_{TD} increases proportionally
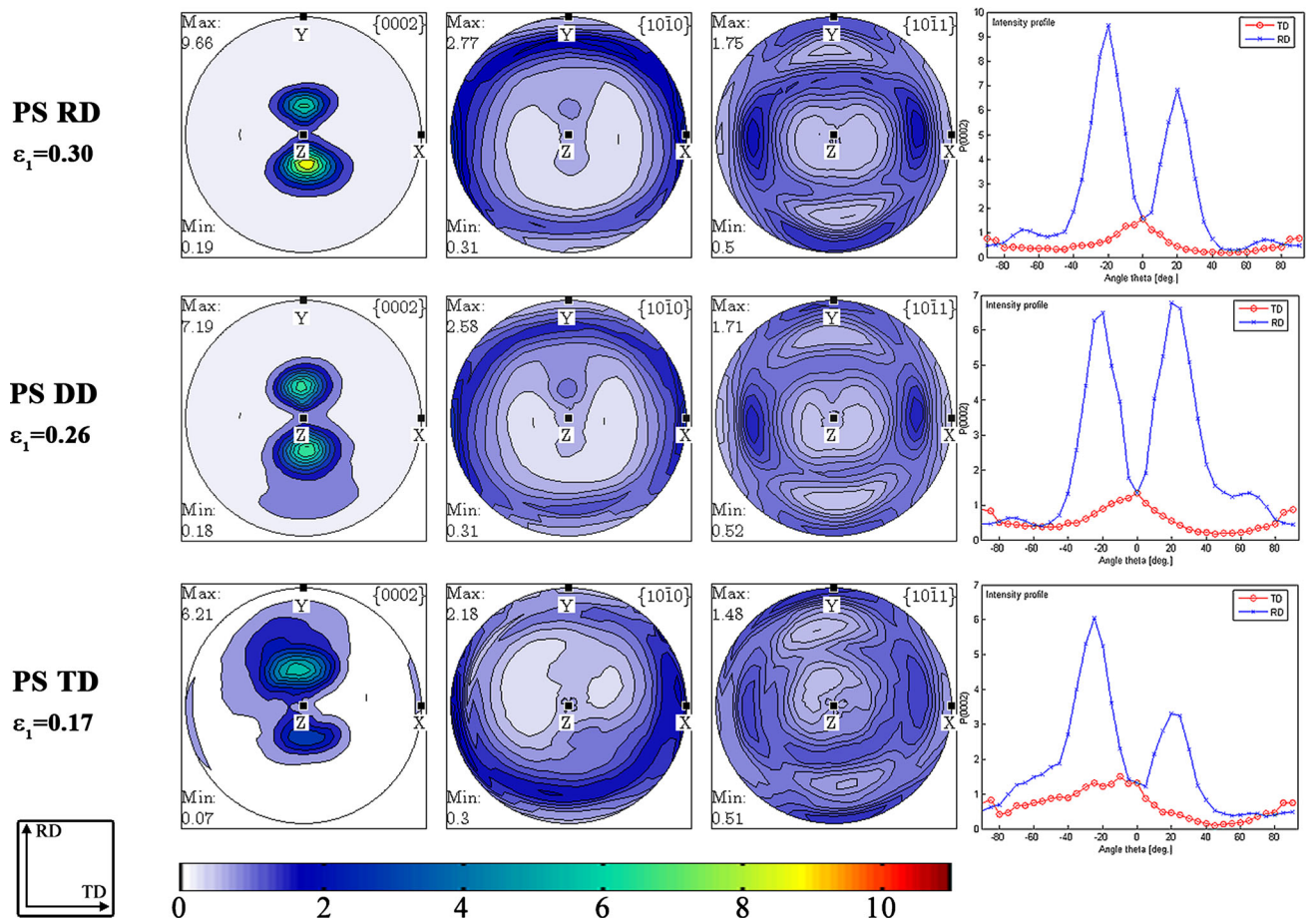
Fig. 11—Pole figures of the PS samples and intensity profiles of the basal poles with respect to RD and TD.

more than f_{RD}, which indicates that the poles are more dispersed in TD than in the as-received condition. Similar trends are found in the DD and TD samples with proportionally higher increases of f_{TD}.

Figure 12 shows the $\varphi_2 = 0$ deg and $\varphi_2 = 30$ deg ODF sections for the specimens that have been deformed in PS conditions until failure. The texture component $\varphi_1 = 0$ deg, $\phi = 20$ deg, $\varphi_2 = 0$ deg, i.e., close to $\{\bar{1}2\bar{1}10\}\langle10\bar{1}0\rangle$, is relatively stable and its intensity grows as deformation increases; this effect is more marked in PS RD than in PS TD. In PS tests, the effect of the sheet orientation on the further evolution of the texture is less intense than in the case of UAT. The {0001} basal fiber present in the three sample directions is not suppressed, in contrast to the UAT TD specimen.

The samples deformed by EBA (Figure 13) also show a decrease in the concentration of basal poles, but maintain the angle to ND. By consequence, f_{ND} decreases. Similarly to UAT and PS, f_{TD} increases proportionally more than f_{RD}.

The ODF after EBA stretching (Figure 14) shows the highest similarity between the two sections, characterized by a high density around the positions defined by $\varphi_1 = 0$ deg, $\phi = 20$ deg, $\varphi_2 = 0$ deg, i.e., $\{\bar{1}2\bar{1}10\}$ $\langle10\bar{1}0\rangle$ and $\varphi_1 = 0$ deg, $\phi = 20$ deg, $\varphi_2 = 30$ deg, i.e., $\{01\bar{1}6\}\langle2\bar{1}\bar{1}0\rangle$.

In general, all deformation conditions applied to the material reduce the intensity of texture. The relative low intensity of the ODF after deformation, with respect to the initial texture, could be related to continuous dynamic recrystallization (cDRX), which is frequently observed in highly deformed HCP metals, e.g., Mg.[26] The microstructure evolution in cDRX results from progressive fragmentation of the grains. First, subgrains are formed because dislocations organize into low-angle boundaries (LAB) (polygonization). Dislocations get continuously accumulated, resulting in a progressive increase of misorientation at the LABs, which evolve into high-angle boundaries (HAB), completing the recrystallization process, which leads

to an intensity decrease of the texture. Although the simulation results are not shown here, the observed crystallographic textures evolution are compatible with VPSC model predictions when the basal slip system is the most favored over the prismatic or the pyramidal ones. Additionally, an extension of the VPSC model that allows to include the effect of subgrain formation[27] is currently being adapted to the specific case

of zinc. This will allow us to account for the influence of cDRX in the intensity of the developed texture. These improvements are in progress and will be reported elsewhere.

IV. CONCLUSIONS

The crystallographic texture evolution of a zinc sheet has been analyzed through the X-ray technique. Different industrial-like processing conditions were considered, as well as different relative orientations between material and loading axes. The zinc alloy sheet has a strong mechanical anisotropy, as evidenced by the stress–strain curves and the Lankford coefficients. The strong texture exhibited by the sheet plays an important role on this behavior.

The crystallographic texture of the as-received Zn20 sheet shows two intense components with the c-axes at 20 deg with respect to ND, contained in the ND–RD plane. The different deformation conditions, imposed by the various strain paths, lead to an intensity decrease of the crystallographic texture of the sheet, as a consequence of dispersion around the c-axes. The strain states applied in this study do not appear to produce the development of new texture components, but they reduce the texture intensity and therefore the mechanical anisotropy of the material. This effect is
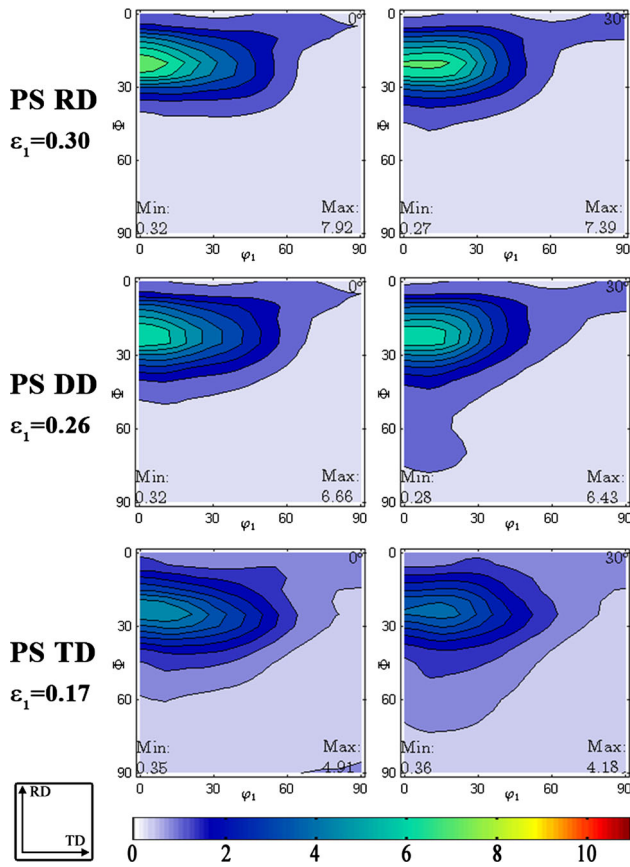

Fig. 12—Sections of the ODF for $\varphi_2 = 0$ deg (left) and $\varphi_2 = 30$ deg (right) for the PS samples.
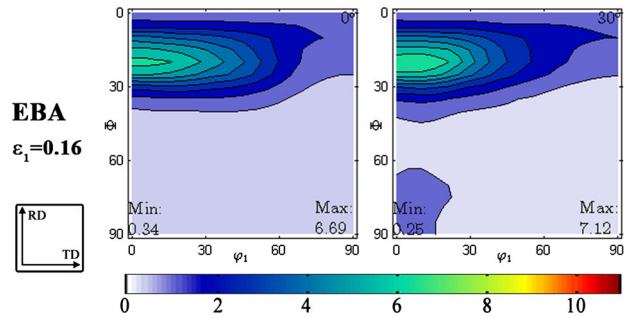

Fig. 14—Sections of the ODF for $\varphi_2 = 0$ deg (left) and $\varphi_2 = 30$ deg (right) for the EBA sample.
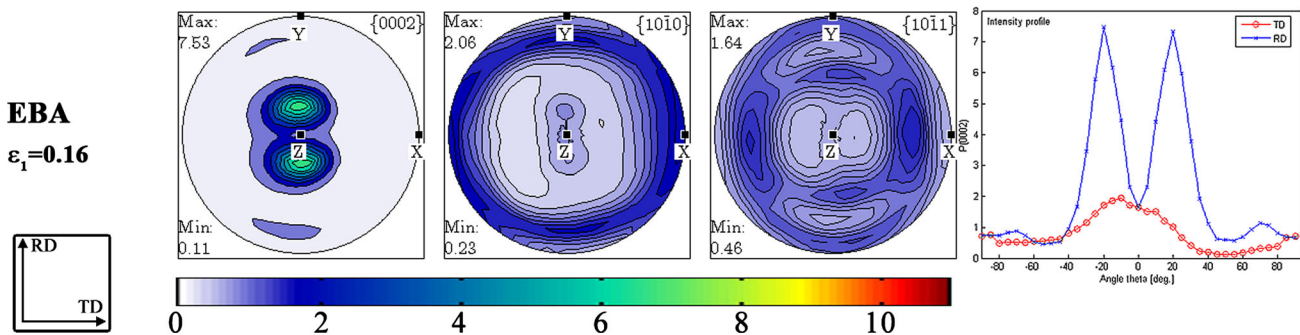

Fig. 13—Pole figures of the EBA sample and intensity profiles of the basal poles with respect to RD and TD.

more marked for the specimens strained along the TD direction.

REFERENCES

1. Y.N. Wang and J.C. Huang: *Mater. Chem. Phys.*, 2003, vol. 81, pp. 11–26.
2. H.S. Rosenbaum: *Acta Metall.*, 1961, vol. 9, pp. 742–48.
3. J.N. Florando, M. Rhee, A. Arsenlis, M.M. Leblanc, and D.H. Lassila: *Philos. Mag. Lett.*, 2006, vol. 86, pp. 795–805.
4. A.N. Bramley and P.B. Mellor: *Int. J. Mech. Sci.*, 1968, vol. 10, pp. 211–19.
5. C. Schwindt, F. Schlosser, M.A. Bertinetti, M. Stout, and J.W. Signorelli: *Int. J. Plasticity*, 2015, vol. 73, pp. 62–99.
6. M.J. Philippe, F. Wagner, F.E. Mellab, C. Esling, and J. Wegria: *Acta Metall. Mater.*, 1994, vol. 42, pp. 239–50.
7. M.A. Valouch: *Metallwisrtsch*, 1932, vol. 11, p. 165.
8. I.L. Dillamore and W.J. Roberts: *Metal Rev.*, 1965, vol. 39, p. 10.
9. M. Diot, J.J. Fundenberger, M.J. Philippe, J. Wégria, and C. Esling: *Scripta Mater.*, 1998, vol. 39, pp. 1623–30.
10. M. Diot, M.J. Philippe, J. Wégria, and C. Esling: *Scripta Mater.*, 1999, vol. 40, pp. 1295–1303.
11. F Zhang, G Vincent, YH Sha, L. Zuo, J.J. Fundenberger, and C. Esling: *Scripta Mater.*, 2004, vol. 50, pp. 1011–15.
12. D.E. Solas, C.N. Tomé, O. Engler, and H.R. Wenk: *Acta Mater.*, 2001, vol. 49, pp. 3791–3801.
13. M. Faur and G. Cosmeleată: *U.P.B. Sci. Bull. Ser. B*, 2006, vol. 68, pp. 67–74.
14. AP Miodownik: *Binary Alloy Phase Diagrams*, 2nd ed., ASM International, Materials Park, 1991.
15. T.H. Muster, W.D. Ganther, and I.S. Cole: *Corros. Sci.*, 2007, vol. 49, pp. 2037–58.
16. Y. Jansen, R.E. Logé, P.-Y. Manach, G. Carbuccia, and M. Milesi: *Int. J. Mater. Form.*, 2016, DOI:10.1007/s12289-016-1313-8.
17. M.A. Sutton, J.-J. Orteu, and H.W. Schreier: *Image Correlation for Shape, Motion and Deformation Measurements, 2009 edition*, Springer, New York, 2009.
18. L. Lutterotti. *Maud (material analysis using diffraction)*, August 2016.
19. D.L. Kaiser, J.R.L. Watters: *Standard reference material ®660b*, 2010.
20. N.C. Popa: *J. Appl. Crystallogr.*, 1998, vol. 31, pp. 176–80.
21. F. Bachmann, R. Hielscher, and H. Schaeben: *Solid State Phenom.*, 2010, vol. 160, pp. 63–68.
22. D. Mainprice, F. Bachmann, R. Hielscher, and H. Schaeben: *Geol. Soc. Spec. Publ.*, 2014, vol. 409, pp. 251–71.
23. J.A. Gruber, S.A. Brown, and G.A. Lucadamo: *J. Nucl. Mater.*, 2011, vol. 408, pp. 176–82.
24. H. Okamoto: *J. Phs. Eqil. and Diff.*, 2008, vol. 29, pp. 211–12.
25. S.W.K. Morgan: *Zinc and Its Alloys and Compounds*, Wiley, New York, 1985, pp. 155–64.
26. A. Jäger, V. Gärtnerová, and T. Mukai: *Mater. Charact.*, 2014, vol. 93, pp. 102–09.
27. J. Signorelli and A. Tommasi: *Earth Planet. Sci. Lett.*, 2015, vol. 430, pp. 356–66.